JACS
JOURNAL OF THE AMERICAN CHEMICAL SOCIETY

Communication

pubs.acs.org/JACS

Site-Specific Substitutional Boron Doping of Semiconducting Armchair Graphene Nanoribbons

Ryan R. Cloke,[†,∥] Tomas Marangoni,[†,∥] Giang D. Nguyen,[‡,∥] Trinity Joshi,[‡] Daniel J. Rizzo,[‡] Christopher Bronner,[‡] Ting Cao,[‡] Steven G. Louie,[‡,§] Michael F. Crommie,*[,‡,§,⊥] and Felix R. Fischer*[,†,§,⊥]

[†]Department of Chemistry and [‡]Department of Physics, University of California Berkeley, Berkeley, California 94720, United States
[§]Materials Sciences Division, Lawrence Berkeley National Laboratory, Berkeley, California 94720, United States
[⊥]Kavli Energy NanoSciences Institute at the University of California Berkeley and the Lawrence Berkeley National Laboratory, Berkeley, California 94720, United States

Supporting Information

ABSTRACT: A fundamental requirement for the development of advanced electronic device architectures based on graphene nanoribbon (GNR) technology is the ability to modulate the band structure and charge carrier concentration by substituting specific carbon atoms in the hexagonal graphene lattice with p- or n-type dopant heteroatoms. Here we report the atomically precise introduction of group III dopant atoms into bottom-up fabricated semiconducting armchair GNRs (AGNRs). Trigonal-planar B atoms along the backbone of the GNR share an empty p-orbital with the extended π-band for dopant functionality. Scanning tunneling microscopy (STM) topography reveals a characteristic modulation of the local density of states along the backbone of the GNR that is superimposable with the expected position and concentration of dopant B atoms. First-principles calculations support the experimental findings and provide additional insight into the band structure of B-doped 7-AGNRs.

Atomically defined graphene nanoribbons (GNRs), two-dimensional configurations of single-layer graphene featuring high aspect ratios, have attracted increased interest for their exotic electronic and magnetic properties emerging from quantum interference effects at the nanometer scale.[1−6] Atomically precise control over the boundary conditions imposed by the width, the crystallographic symmetry, and the edge structure of GNRs is paramount for the rational design of device-critical parameters such as the band gap, the Fermi level, and the position and concentration of dopant atoms.[7−14] Recent advances in the bottom-up fabrication of atomically precise GNRs from molecular precursors have demonstrated the rational modulation of the width, the symmetry, the edge structure (armchair, chevron, cove), and the incorporation of nitrogen atom dopants in the form of pyridine and pyrimidine rings into the edges of chevron-GNRs.[15−22] Since the lone-pair of the N-heteroatom in these structures is not in conjugation with the extended π-system of the GNR, edge-doping only shifts the position of both the conductance and valence band edges of the ribbon without introducing dopant states into the gap.[20] Controlled n-/p-doping, i.e., the controlled introduction of filled/empty donor or acceptor states into the gap of atomically defined GNRs, instead requires the incorporation of dopant heteroatoms at precise positions along the backbone of the ribbon where the filled/empty p-orbitals are in conjugation with the extended π-system.

Here we report the bottom-up synthesis and characterization of atomically defined hydrogen terminated n = 7 armchair GNRs (7-AGNRs, n corresponds to the number of carbon atoms across the width of the ribbon) featuring a regioregular pattern of B atoms along the central backbone of the ribbon. We performed the thermally induced radical step-growth polymerization/cyclization of the molecular precursor, 5,10-bis(10-bromoanthracene-9-yl)-5,10-dihydroboranthrene (**1**, Figure 1a), on Au(111) in ultra-high vacuum (UHV). Low-temperature scanning tunneling microscopy (STM) imaging of fully cyclized B-doped 7-AGNRs (B-7AGNRs) reveals a unique, characteristic stripe pattern along the length of the ribbon with a period corresponding to the distance between the expected position of dopant atoms in the molecular repeat unit (Figure 1d,e). This is consistent with the empty p-orbitals of boron conjugating to the extended π-system of the 7-AGNR and acting as substitutional dopants. Density functional theory (DFT) calculations reveal that B-7AGNRs have a deep acceptor band at energies within the gap of undoped 7-AGNRs, which is localized along the backbone of a B-7AGNR and verified experimentally through dI/dV imaging.

The boron-doped 7-AGNR precursor **1** (Figure 1a) was obtained through selective monolithiation of 9,10-dibromoanthracene (**2**), followed by borylation with 5,10-dibromo-5,10-dihydroboranthrene (**3**) in 73% yield (Figure 2). Despite the reported instability of this class of substituted boranthrenes, crystals of **1** are stable in air at 24 °C showing no signs of degradation over several months, as indicated by ^{1}H NMR spectroscopy (Supporting Information (SI), Figure S1).[23−25] DSC and TGA analysis reveals a melting point above 350 °C and a gradual mass loss associated with partial dehalogenation above this temperature (SI, Figure S2).

Received: March 11, 2015
Published: July 8, 2015

DOI: 10.1021/jacs.5b02523
J. Am. Chem. Soc. 2015, 137, 8872−8875

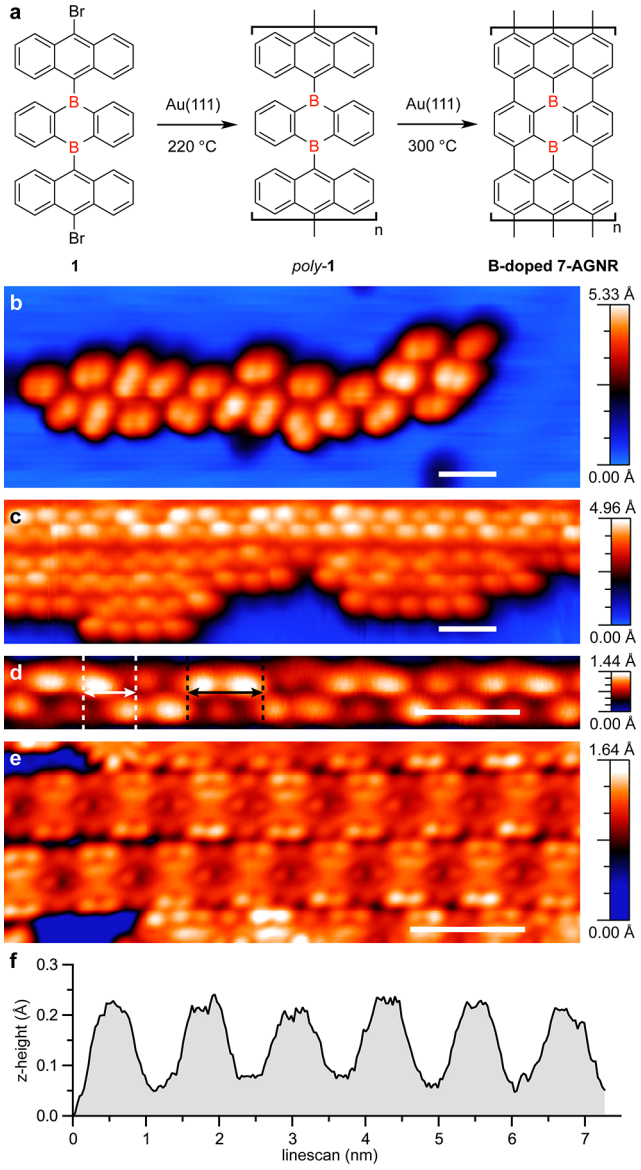

Figure 1. (a) Schematic representation of the bottom-up synthesis of B-7AGNRs. (b) STM topographic image of molecular building block **1** as deposited onto a pristine Au(111) surface held at 24 °C (sample voltage V_s = 1.5 V, tunneling current I_t = 30 pA, imaging temperature T = 13 K). Subsequent annealing steps induce the homolytic cleavage of the labile C−Br bonds, followed by radical step-growth polymerization (220 °C) and thermal cyclization/dehydrogenation (300 °C) to yield B-7AGNRs. (c) STM topographic image of *poly*-**1** (V_s = 1.0 V, I_t = 20 pA, T = 13 K). (d) STM topographic image of poly-**1** showing a characteristic pattern of alternating protrusions (V_s = 1.0 V, I_t = 20 pA, T = 13 K). (e) STM topographic image of fully cyclized B-7AGNRs (V_s = −0.1 V, I_t = 3 pA, T = 4.5 K). (f) Representative z-axis profile showing the characteristic height modulation along the long axis of a B-7AGNR. Scale bar is 2 nm.

Orange crystals of **1** suitable for X-ray diffraction were obtained by slow evaporation of a $C_2H_2Cl_4$ solution. **1** adopts a C_i symmetry in the crystal lattice. The geometry around the boron atom is trigonal-planar with bond angles and bond distances ranging between 119.7−120.9° and 1.56−1.78 Å, respectively. While the two 9-bromoanthracene units are coplanar, the central boranthrene is twisted out of planarity with a dihedral angle C(2)−C(1)−B(1)−C(15) = 97.6° (Figure 2). This nonplanar conformation is crucial as it

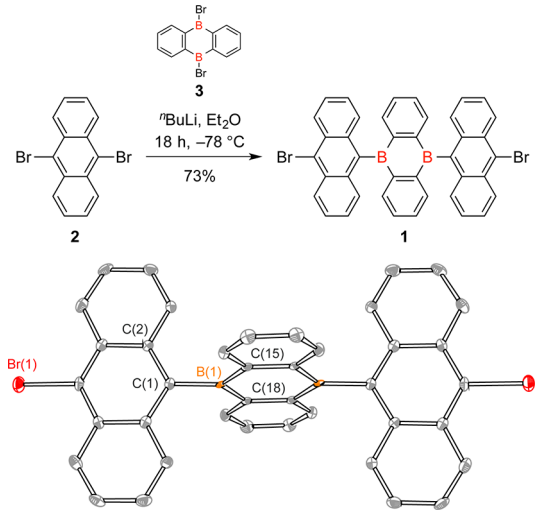

Figure 2. Synthesis of the B-doped molecular precursor **1** (top). ORTEP representation of the X-ray crystal structure of **1** (bottom). Thermal ellipsoids are drawn at the 50% probability level. Color coding: C (gray), Br (red), B (orange). Hydrogen atoms and cocrystallized solvent molecules are omitted for clarity. Relevant structural parameters: C(1)−B(1), 1.578(5) Å; C(15)−B(1), 1.561(5) Å; C(18)−B(1), 1.562(5) Å; C(2)−C(1)−B(1)−C(15), 97.6°; $C_{46}H_{30}B_2Br_2Cl_{12}$; 1189.54 g mol^{-1}; triclinic; P−1; orange; a = 8.6046(3) Å; b = 9.8632(4) Å; c = 14.5013(6) Å; α = 82.148(2)°, β = 82.067(2)°; γ = 74.011(2)°; 100 (2) K; Z = 1; R1 = 0.0387; GOF on F^2 = 1.036.

sterically shields the Lewis acidic B atoms from nucleophilic attack and imparts a favorable nonplanar geometry to the molecule, a prerequisite for an efficient radical step-growth polymerization on the Au(111) substrate.[1,15−21,26−29]

Fully cyclized B-7AGNRs were fabricated by sublimation of molecular building block **1** at 250−270 °C in UHV onto pristine Au(111) held at 24 °C. STM imaging at 13 K prior to polymerization reveals that the molecules assemble into irregular islands with an apparent height of 0.4 nm (Figure 1b), clustered around the Au(111) herringbone reconstruction. Gradual annealing of submonolayer samples of **1** on Au(111) to 220 °C (20 min) induces homolytic cleavage of the labile C−Br bond, followed by step-growth polymerization of the carbon-centered diradical intermediates to form extended linear polymer chains *poly*-**1** (Figure 1c). STM images of polymer chains display a characteristic pattern of alternating protrusions (average distance between white markers 0.95 ± 0.04 nm, Figure 1d) along the polymer backbone. The repulsive interaction between *peri*-hydrogen atoms in adjacent anthracene units prevents a coplanar arrangement of monomer units in the polymer backbone (this observation is consistent with images of polyanthracene, the precursor to undoped 7-AGNRs).[1,26,27] Unique to the B-doped GNR precursors is a distinctive secondary structure along the polymer that correlates with the length of a monomer unit (Figure 1a) in *poly*-**1** (average distance between black markers 1.40 ± 0.04 nm, Figure 1d). While the anthracene fragments appear as brighter spots in topographic STM images, the more electron-deficient boranthrenes correlate with a weaker signal that alternates along the edges of the polymer. The observation of this characteristic secondary pattern in images of *poly*-**1** indicates that the exocyclic B−C bonds are stable under the polymerization conditions and no undesired fragmentation of

DOI: 10.1021/jacs.5b02523
J. Am. Chem. Soc. 2015, 137, 8872−8875

monomer building blocks is observed during the step-growth process.

Further annealing of the Au(111) substrate at 300 °C (20 min) induces a thermal cyclization/dehydrogenation sequence that converts *poly*-**1** into fully conjugated B-7AGNRs (Figure 1e). The apparent width and average height of the resulting GNRs are 1.6 nm and 0.16 ± 0.04 nm, respectively. Statistical analysis of large area STM images of densely packed ribbons shows that the majority of B-7AGNRs ranges in length between 4−12 nm with a few examples exceeding 16 nm (SI, Figure S5). STM topography at negative bias reveals a characteristic stripe pattern corresponding to a height modulation (amplitude 0.14 ± 0.02 Å) along the length of the B-7AGNRs (Figure 1f). The periodicity of this topographic feature, 1.30 ± 0.05 nm, correlates with the expected spacing between boranthene units along the backbone of a B-7AGNR (Figure 1a).

In order to better understand the electronic effects of substitutive B-doping in B-7AGNRs, we performed first-principles calculations based on the GW approximation and included the screening effects from the underlying Au(111) substrate (see SI for computational details).[16] The total density of states (DOS) at the GW level for a B-7AGNR is depicted in Figure 3a. The DOS of both the valence (VB) and the conduction (CB) bands show significant contributions (∼10%) from B atoms. Comparing to the electronic structure of a pristine 7-AGNR (Figure 3a), substitutive B-doping along the backbone of a 7-AGNR introduces a deep acceptor band (CB) 0.8 eV above the VB maximum. The theoretically predicted quasiparticle band gap of B-7AGNRs, 0.8 eV (Figure 3b), is significantly smaller than that of the undoped 7-AGNRs (∼2.1 eV) calculated with the same method (the undoped 7-AGNR DOS is shown in Figure 3a).

The spatial distribution of the states associated with both the conductance band (CB) and the CB+1 band was investigated by dI/dV mapping. Figure 3c shows a B-7AGNR dI/dV map at V_s = 1.0 V, corresponding to states in the CB. The dI/dV map shows a predominance of local density of states (LDOS) along the backbone of the ribbon. This can be compared to the CB LDOS map calculated for a given energy range at a distance of 4 Å above a B-7AGNR plane (Figure 3d). In strong contrast to undoped 7-AGNRs,[27] both the experimental and theoretical LDOS maps at this energy show significant higher state density along the backbone of the B-7AGNR. Atomic scale features are not well-resolved experimentally, likely due to tip-induced broadening and substrate interactions that are not accounted for in the calculation. The dI/dV map recorded at a higher bias of V_s = 1.6 V (corresponding to an energy closer to CB+1) shows strong localization of the LDOS along the edges of the B-7AGNR (Figure 3e). This agrees with the calculated LDOS map of B-7AGNR CB+1 states (Figure 3f) and is reminiscent of bandedge LDOS observed in undoped 7-AGNRs.[27] These spectroscopic maps provide additional evidence that the substitution of C atoms with trigonal planar B atoms in GNRs induces a change in their electronic structure.

In conclusion, we demonstrate atomically precise bottom-up synthesis of 7-AGNRs with dopant atoms inserted directly into the GNR backbone. The trigonal planar B atoms incorporated at defined positions along the GNR share an empty p-orbital with the extended π-system, potentially providing hole dopant concentrations in excess of 10^{14} cm^{-2}. The highly regular placement of p-dopants along the 7-AGNR is reflected in a characteristic modulation of the LDOS along the backbone of the ribbon visualized by STM topographic imaging. Such site-specific substitutional doping of GNRs with group III heteroatoms will help pave the way toward the development of advanced functional device architectures based on GNR semiconductor technology.

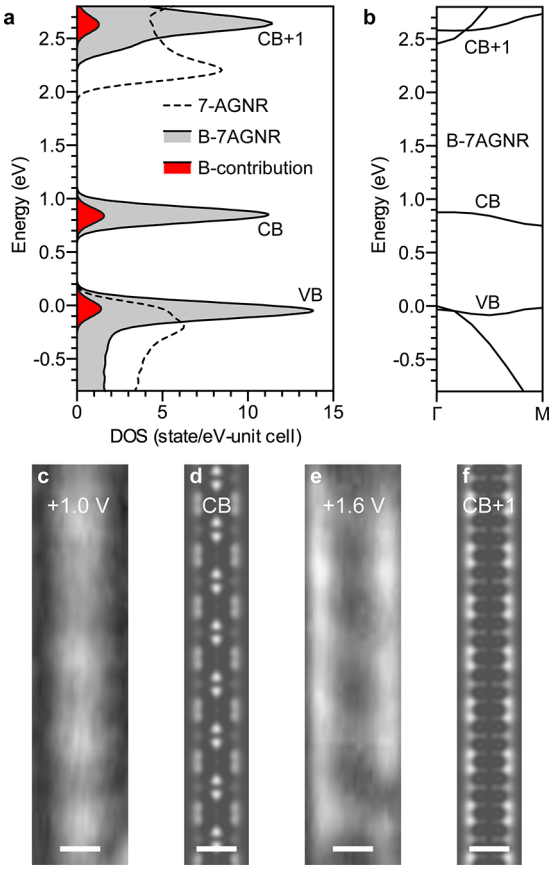

Figure 3. (a) Calculated total DOS for B-7AGNRs (gray) and contribution from B atoms to the DOS (red) using the GW approximation and including screening effects from Au(111) substrate. The total DOS for undoped 7-AGNRs is plotted as a dotted line. A Gaussian broadening of 0.1 eV is applied. The valence band maximum is set to 0 eV. (b) Calculated quasiparticle band structure of B-7AGNRs (using GW approximation). (c) dI/dV spatial map of B-7AGNR recorded at 1.0 V (I_t = 30 pA, modulation voltage V_{rms} = 15 mV, modulation frequency 634 Hz, T = 13 K). (d) Calculated LDOS map of states at the conduction bandedge (CB) at a height of 4 Å above a B-7AGNR plane. (e) dI/dV spatial map of same B-7AGNR as in (c) recorded at 1.6 V (I_t = 30 pA, modulation voltage V_{rms} = 15 mV, modulation frequency 634 Hz, T = 13 K). (f) Calculated LDOS maps of CB+1 bandedge states at a height of 4 Å above a B-7AGNR plane. Calculated images average states over an energy range of 0.1 eV, scale bar 1 nm.

■ ASSOCIATED CONTENT

Supporting Information

Figures S1−S3, S5; methods and instrumentation; synthetic procedure and characterization of **1**; X-ray crystallographic data (Figure S4, Tables S1−S5 and CIF); NMR spectra (Figure S6−S8). The Supporting Information is available free of charge on the ACS Publications website at DOI: 10.1021/jacs.5b02523.

■ AUTHOR INFORMATION

Corresponding Authors

*crommie@berkeley.edu
*ffischer@berkeley.edu

DOI: 10.1021/jacs.5b02523
J. Am. Chem. Soc. 2015, 137, 8872−8875

Author Contributions

[‖]R.R.C., T.M., and G.D.N. contributed equally.

Notes

The authors declare no competing financial interest.

■ ACKNOWLEDGMENTS

Research supported by the U.S. Department of Energy (DOE), Office of Science, Basic Energy Sciences (BES), under award no. DE-SC0010409 (design, synthesis, and characterization of molecular building blocks) and Nanomachine Program award no. DE-AC02-05CH11231 (surface reaction characterization and STS image simulations), by the Office of Naval Research BRC Program (GNR characterization), by the National Science Foundation (NSF) award no. DMR-1206512 (image analysis), and DMR10-1006184 (basic theory and formalism). Berkeley NMR Facility is supported in part by NIH grant SRR023679A. X-ray Facility is supported in part by NIH Shared Instrumentation grant S10-RR027172, computational resources were provided by the NSF through XSEDE resources at the Texas Advanced Computing Center (TACC) at the University of Texas at Austin and NERSC at the Lawrence Berkeley National Laboratory. T.J. acknowledges support from NSF Graduate Research Fellowship Program under grant no. DGE 1106400. C.B. acknowledges support through the Fellowship Program of the German National Academy of Sciences Leopoldina under grant no. LPDS 2014-09. The authors acknowledge Dr. Antonio DiPasquale for assistance with X-ray analysis and Won-Woo Choi, Hsin-Zon Tsai, Arash A. Omrani, and Han Sae Jung for their technical assistance.

■ REFERENCES

(1) Cai, J.; Ruffieux, P.; Jaafar, R.; Bieri, M.; Braun, T.; Blankenburg, S.; Muoth, M.; Seitsonen, A. P.; Saleh, M.; Feng, X.; Müllen, K.; Fasel, R. *Nature* **2010**, *466*, 470−473.
(2) Kim, W. Y.; Kim, K. S. *Nat. Nanotechnol.* **2008**, *3*, 408−412.
(3) Son, Y. W.; Cohen, M. L.; Louie, S. G. *Nature* **2006**, *444*, 347−349.
(4) Barone, V.; Hod, O.; Scuseria, G.-E. *Nano Lett.* **2006**, *6*, 2748−2754.
(5) Zhang, X.; Yazyev, O. V.; Feng, J.; Xie, L.; Tao, C.; Chen, Y.-C.; Jiao, L.; Pedramrazi, Z.; Zettl, A.; Louie, S. G.; Dai, H.; Crommie, M. F. *ACS Nano* **2013**, *7*, 198−202.
(6) Son, Y.-W.; Cohen, M. L.; Louie, S. G. *Phys. Rev. Lett.* **2006**, *97*, 216803.
(7) Koch, M.; Ample, F.; Joachim, C.; Grill, L. *Nat. Nanotechnol.* **2012**, *7*, 713−717.
(8) Terrones, H.; Lv, R.; Terrones, M.; Dresselhaus, M. *Rep. Prog. Phys.* **2012**, *75*, 062501.
(9) Martins, T. B.; Miwa, R. H.; da Silva, A. J. R.; Fazzio, A. *Phys. Rev. Lett.* **2007**, *98*, 196803.
(10) Yan, Q.; Huang, B.; Yu, J.; Zheng, F.; Zang, J.; Wu, J.; Gu, B.-L.; Liu, F.; Duan, W. *Nano Lett.* **2007**, *7*, 1469−1473.
(11) Avouris, P.; Chen, Z.; Perebeinos, V. *Nat. Nanotechnol.* **2007**, *2*, 605−615.
(12) Qi, Z. J.; Rodríguez-Manzo, J. A.; Botello-Méndez, A. R.; Hong, S. J.; Stach, E. A.; Park, Y. W.; Charlier, J.-C.; Drndić, M.; Johnson, A. T. C. *Nano Lett.* **2014**, *14*, 4238−4244.
(13) Pan, M.; Girão, E. C.; Jia, X.; Bhaviripudi, S.; Li, Q.; Kong, J.; Meunier, V.; Dresselhaus, M. S. *Nano Lett.* **2012**, *12*, 1928−1933.
(14) Tao, C.; Jiao, L.; Yazyev, O. V.; Chen, Y.-C.; Feng, J.; Zhang, X.; Capaz, R. B.; Tour, J. M.; Zettl, A.; Louie, S. G.; Dai, H.; Crommie, M. F. *Nat. Phys.* **2011**, *7*, 616−620.
(15) Chen, Y.-C.; de Oteyza, D. G.; Pedramrazi, Z.; Chen, C.; Fischer, F. R.; Crommie, M. F. *ACS Nano* **2013**, *7*, 6123−6128.
(16) Chen, Y.-C.; Cao, T.; Chen, C.; Pedramrazi, Z.; Haberer, D.; de Oteyza, D. G.; Fischer, F. R.; Louie, S. G.; Crommie, M. F. *Nat. Nanotechnol.* **2015**, *10*, 156−160.
(17) Basagni, A.; Sedona, F.; Pignedoli, C. A.; Cattelan, M.; Nicolas, L.; Casarin, M.; Sambi, M. *J. Am. Chem. Soc.* **2015**, *137*, 1802−1808.
(18) Narita, A.; Verzhbitskiy, I. A.; Frederickx, W.; Mali, K. S.; Jensen, S. A.; Hansen, M. R.; Bonn, M.; De Feyter, S.; Casiraghi, C.; Feng, X.; Müllen, K. *ACS Nano* **2014**, *8*, 11622−11630.
(19) Talirz, L.; Söde, H.; Cai, J.; Ruffieux, P.; Blankenburg, S.; Jafaar, R.; Berger, R.; Feng, X.; Müllen, K.; Passerone, D.; Fasel, R.; Pignedoli, C. A. *J. Am. Chem. Soc.* **2013**, *135*, 2060−2063.
(20) Cai, J.; Pignedoli, C. A.; Talirz, L.; Ruffieux, P.; Söde, H.; Liang, L.; Meunier, V.; Berger, R.; Li, R.; Feng, X.; Müllen, K.; Fasel, R. *Nat. Nanotechnol.* **2014**, *9*, 896−900.
(21) Bronner, C.; Stremlau, S.; Gille, M.; Brausse, F.; Haase, A.; Hecht, S.; Tegeder, P. *Angew. Chem., Int. Ed.* **2013**, *52*, 4422−4425.
(22) Vo, T. H.; Shekhirev, M.; Kunkel, D. A.; Morton, M. D.; Berglund, E.; Kong, L.; Wilson, P. M.; Dowben, P. A.; Enders, A.; Sinitskii, A. *Nat. Commun.* **2014**, *5*, 1−8.
(23) Bieller, S.; Zhang, F.; Bolte, M.; Bats, J. W.; Lerner, H.-W.; Wagner, M. *Organometallics* **2004**, *23*, 2107−2113.
(24) Hoffend, C.; Schödel, F.; Bolte, M.; Lerner, H.-W.; Wagner, M. *Chem. - Eur. J.* **2012**, *18*, 15394−15405.
(25) Dou, C.; Saito, S.; Matsuo, K.; Hisaki, I.; Yamaguchi, S. *Angew. Chem., Int. Ed.* **2012**, *51*, 12206−12210.
(26) Blankenburg, S.; Cai, J.; Ruffieux, P.; Jaafar, R.; Passerone, D.; Feng, X.; Müllen, K.; Fasel, R.; Pignedoli, C. A. *ACS Nano* **2012**, *6*, 2020−2025.
(27) Ruffieux, P.; Cai, J.; Plumb, N. C.; Patthey, L.; Prezzi, D.; Ferretti, A.; Molinari, E.; Feng, X.; Müllen, K.; Pignedoli, C. A.; Fasel, R. *ACS Nano* **2012**, *6*, 6930−6935.
(28) Batra, A.; Cvetko, D.; Kladnik, G.; Adak, O.; Cardoso, C.; Ferretti, A.; Prezzi, D.; Molinari, E.; Morgante, A.; Venkataraman, L. *Chem. Sci.* **2014**, *5*, 4419−4423.
(29) Bronner, C.; Björk, J.; Tegeder, P. *J. Phys. Chem. C* **2015**, *119*, 486−493.

DOI: 10.1021/jacs.5b02523
J. Am. Chem. Soc. 2015, 137, 8872−8875